A new framework for quantifying alongshore variability of swash motion using fully convolutional networks

Reza Salatin [a], Qin Chen [b,*], Britt Raubenheimer [a], Steve Elgar [a], Levi Gorrell [a], Xin Li [c]

[a] *Woods Hole Oceanographic Institution, Woods Hole, MA, 02543, USA*
[b] *Department of Civil and Environmental Engineering, Department of Marine and Environmental Sciences, Northeastern University, Boston, MA, 02115, USA*
[c] *Section of Visual Computing and Computational Media, School of Performance, Visualization, and Fine Arts, Texas A&M University, College Station, TX, 77843, USA*

ARTICLE INFO

ABSTRACT

Waves running up and down the beach ('swash') at the landward edge of the ocean can cause changes to the beach topology, can erode dunes, and can result in inland flooding. Despite the importance of swash, field observations are difficult to obtain in the thin, bubbly, and potentially sediment laden fluid layers. Here, swash excursions along an Atlantic Ocean beach are estimated with a new framework, V-BeachNet, that uses a fully convolutional network to distinguish between sand and the moving edge of the wave in rapid sequences of images. V-BeachNet is trained with 16 randomly selected and manually segmented images of the swash zone, and is used to estimate swash excursions along 200 m of the shoreline by automatically segmenting four 1-h sequences of images that span a range of incident wave conditions. Data from a scanning lidar system are used to validate the swash estimates along a cross-shore transect within the camera field of view. V-BeachNet estimates of swash spectra, significant wave heights, and wave-driven setup (increases in the mean water level) agree with those estimated from the lidar data.

1. Introduction

Waves running up and down the beach ('swash') can lead to beach erosion and wave overtopping (Dodd, 1998; Ruggiero et al., 2001), and when combined with tides and storm surge, can result in coastal flooding and damage to structures (Xie et al., 2019; den Bieman et al., 2020). Obtaining in situ observations of swash in the field is difficult owing to the thin, moving, turbulent fluid layers (Suhayda, 1974; Guza and Thornton, 1985; Raubenheimer et al., 1995). Thus, remote sensing approaches often have been used (Holman et al., 1993; Ruggiero et al., 2001; Jensen et al., 2003; Stockdon et al., 2006, 2014; Holman and Stanley, 2007; Vousdoukas et al., 2009; Drummond et al., 2015; Yang et al., 2022). However, despite the advantages of remote sensing techniques in obtaining high-quality data over a large area, analysis remains a challenging and laborious task. Methods to identify swash motions in remotely sensed data include manual discretization and edge detection, and motion detection algorithms (Stockdon et al., 2006, 2014; Vousdoukas et al., 2009; Yang et al., 2022).

Some of the limitations associated with traditional analysis of remotely sensed data can be overcome with deep learning techniques, such as Fully Convolutional Networks (FCNs) (Long et al., 2015). FCNs allow for the processing of entire images of differing sizes in a single forward pass, making them more effective than traditional classification techniques such as Support Vector Machines (SVMs) (Cortes and Vapnik, 1995), Random Forests (Breiman, 2001), and CNNs (Krizhevsky et al., 2012; LeCun et al., 2015) for tasks requiring detailed spatial analysis. This efficiency and flexibility make FCNs particularly suited for high-resolution, pixel-level image segmentation and classification in remote sensing. FCNs, however, are memory intensive because they maintain detailed feature maps at a range of scales throughout the network to capture both the fine details and the broader context of the images. The Adaptive Feature Bank (Liang et al., 2020a, 2023), a matching-based framework for semi-supervised video object segmentation, not only dynamically absorbs new features and discards obsolete ones for efficient and flexible video object segmentation, but also outperforms other state-of-the-art methods in terms of accuracy, efficiency, and memory usage on several benchmark datasets, all while allowing for real-time processing of large datasets. Recently, emerging models like the Segment Anything Model (SAM) (Kirillov et al., 2023) are revolutionizing the field of image processing, offering impressive performance on segmentation of new images in a user-friendly environment.

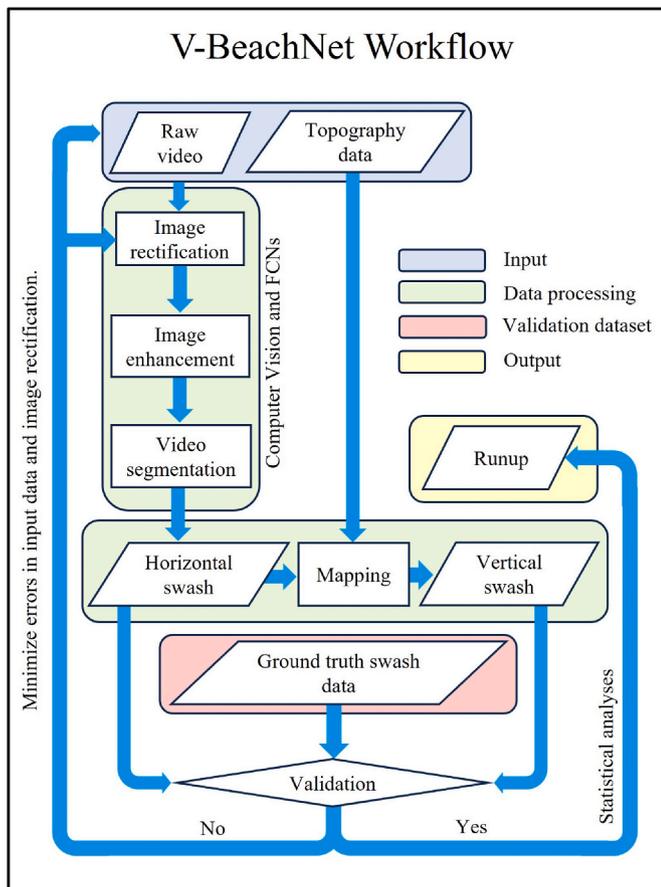Recent applications of deep learning techniques have contributed

Fig. 1. V-BeachNet workflow illustrating the necessary steps to obtain along-shore wave runup data from raw video imagery.

significantly to the understanding of hydrodynamic phenomena, including flood inundation and the spatial distribution of hazards (Jafari et al., 2021; Bentivoglio et al., 2022), dynamics in wave flumes (den Bieman et al., 2020), and beach state classifications (Ellenson et al., 2020). Here, a novel deep learning framework, V-BeachNet, is developed to estimate swash excursions on beaches, using observations from an Atlantic Ocean beach on the Outer Banks of North Carolina. Utilizing a Fully Convolutional Network (FCN) model, V-BeachNet extracts swash motion from raw video imagery with pixel-level accuracy, providing the ability to estimate swash excursions along the shoreline throughout the camera field of view. By enabling the application of this framework to both archived and real-time video footage, the workflow serves as a useful guide for future studies on quantifying swash using computer vision algorithms. The results not only serve as a valuable validation dataset for phase-resolving numerical modeling (Salatin et al., 2021) but also deepen understanding of alongshore variability of swash motion.

The structure of this paper is outlined as follows. Section 2 provides details on the methodology, including the study location, data collection, and image processing. A high-level explanation of the FCN model is also provided in this section. In Section 3, the results are presented, including video segmentation using FCNs, a comparison of swash measurements between lidar and FCN at a cross-shore transect, and an assessment of the alongshore variation of swash extracted by the V-BeachNet. Discussion on the sources of error in comparison with the lidar measurement also is provided. Section 4 concludes with remarks on this study and recommendations for future research.

2. Methods

2.1. Workflow

Although each step in the process of obtaining runup from raw video imagery is explained in subsequent sections, an overview is given here (Fig. 1). Raw data (blue box in Fig. 1) is processed (green boxes) to obtain horizontal and vertical swash motions. Processed data are validated against ground truth data (red box). Validated data are statistically analyzed to get alongshore wave runup (yellow box).

Input data include raw video imagery and topography measurements. Raw video imagery is rectified to facilitate accurate extraction of swash motion. Here, image rectification is conducted assuming a flat plane at elevation $z = 0$ m. However, topography data can be used to correct distortions caused by assuming a flat plane. The contrast and brightness of rectified images also are improved through image enhancement. Final video images are then semantically segmented by V-BeachNet to obtain horizontal swash motion.

Horizontal swash motion is mapped to the topography to obtain the vertical swash motion. Both the horizontal and vertical swash motion data are compared with ground truth data, which are available for a single cross-shore transect. In the event of any discrepancies between these datasets, it is necessary to identify and resolve any sources of error that may have arisen during the topography survey and image rectification processes (Hughes et al., 2006).

The conventional 2% exceedance of wave runup (R2%) in a random swash time series at any cross-shore transect along the shoreline can be obtained by performing statistical analysis on the validated vertical swash time series. This analysis results in a reliable and robust estimation of wave runup along the entire shoreline.

2.2. Study location and data collection

Observations were obtained along a relatively straight beach on the Outer Banks of North Carolina at the US Army Corps of Engineers Field Research Facility (FRF) in Duck in fall 2021. The facility includes an array of pressure sensors in ~9-m water depth that provides estimates of the frequency-directional spectrum of the incident wave field and a tide gage located on a pier in ~6 m depth (NOAA water level station 8651370).

A lidar system was deployed from late August to November 2021 on a small tower-like platform located about 30 m onshore of the mid-tide water line and overlooking the beach. The lidar system emitted a laser beam that scanned along a cross-shore transect near alongshore distance Y = 620 m at 5 Hz for 40 min every hour, followed by a 360-degree rotating scan to estimate the surrounding topography. Here, the cross-shore scans are used to detect the edge of the swash as it runs up and down the beach, and to provide an estimate of the underlying topography. A 0.03 m minimum water depth is used to detect the edge of the swash (O'Dea et al., 2019; Collins et al., 2023). Combining lidar estimates of the horizontal swash with the elevation of the beach provides estimates of the vertical swash elevations.

Sequences of images were obtained from two cameras mounted on a 40-m tall tower located about 60 m onshore of the mid-tide water line near cross-shore and alongshore position X = 35, Y = 585 m. The cameras were sampled at 2 Hz and had overlapping fields of view. Images were corrected for camera curvature and geo-rectified using ground control points, The rectification procedure assigns real-world horizontal cross- (X) and alongshore (Y) coordinates to the images, assuming a constant vertical elevation. Rectified images covered 100 m in the cross-shore (X) and 200 m in the alongshore (Y) direction. Images were interpolated to a 0.1 by 0.1 m grid. However, the spatial resolution of the raw images decreases with distance from the cameras, which were located near the bottom-left corner of the rectified images. Moreover, the assumption of a flat plane introduces errors in the estimates of swash excursions, as discussed below.

Table 1
Wave Parameters and Mean Water Level for four case studies.

Case	Video Footage Timestamps [a]	lidar Survey Time [a] Vehicle Survey Date	T_{mean}	H_{m0}	MWL[b]	θ_{mean}[c]
1	2021-10-10, 12:00	2021-10-09, 17:00 2021-10-13	7.5 s	2.7 m	0.6 m	−4°
2	2021-10-13, 21:00	2021-10-13, 21:00 2021-10-13	7.9 s	1.0 m	0.5 m	11°
3	2021-10-17, 13:00	2021-10-17, 13:00 2021-10-16	5.9 s	1.3 m	0.3 m	33°
4	2021-10-17, 14:00	2021-10-17, 14:00 2021-10-16	5.8 s	1.3 m	0.1 m	34°

[a] UTC.
[b] NOAA, NAVD88.
[c] Relative to shore normal.

Here, four 1-h video recordings were selected to represent a range of wave and water level conditions. The offshore (~9-m water depth) significant wave heights ranged from 1.0 to 2.5 m, the mean spectral periods ranged from 5.5 to 7.5 s, and wave directions ranged from 34-deg from north of shore normal to 4-deg south of shore normal (Table 1 and Fig. 2), with a range of spectral shapes (Fig. 3). The first case occurred during a storm on a rising tide, whereas the other cases are during milder wave conditions with falling tides (Fig. 2a–d).

Topography (and bathymetry) were estimated using several techniques. The hourly 3D lidar scans provide estimates of the topography above the water level, and for the falling tides during Cases 2, 3, and 4, the 3D surveys immediately following the image sequences provided reasonable coverage of the swash zone. During Case 1, water covered the beach over most of the field of view owing to the rising tide and storm setup, and a prior lidar survey at a lower water level was used to obtain more coverage of the dry beach (Table 1).

The 3D lidar-scan estimates of the topography were extended both cross- (into the water) and alongshore with hydrographic surveys along cross-shore transects spaced 46 m in the alongshore performed by the FRF with an amphibious vehicle. The two surveys were merged and interpolated to a 0.1 m by 0.1 m grid (Fig. 4).

In addition, the lidar cross-shore scans at Y = 620 m can be used to estimate the underlying topography by assuming that the lowest elevation values over a period are sand (reflections from water would be higher) (Collins et al., 2023) (Fig. 5). Although errors may arise owing to changing sand levels over the 40-min scan period, the topography estimated from the scans is collected simultaneously with the swash measurements along the same transect and extends across the entire swash

zone. In contrast, depending on the rate of the falling tide, the dry beach covered by the 3D lidar may not encompass the entire swash zone, and the vehicle surveys are interpolated to Y = 620 m. Thus, the sand levels estimated from the scans may be more accurate than the larger-scale topography surveys. Case 1 exhibits the largest difference (~0.2 m at MWL) between the two survey estimates (Fig. 5a), which is attributed primarily to the 5-h gap between the lidar frame-scan survey and the lidar line-scan survey and will introduce errors when converting horizontal to vertical swash excursions. Cases 2 and 4 also have differences as large as 0.2 m (Fig. 5b–d), but these differences are below MWL, and thus errors in runup will not be as large as those in Case 1. For Case 3, the two estimates of topography are similar (Fig. 5c).

2.3. Image processing and fully convolutional networks

In this system, we employed several enhancement techniques to improve the quality of the images by increasing their contrast and brightness. To suppress the noise signal from the static background such as the dry beach, wave foam, and debris, and to highlight the dynamic characteristics of the scene, such as the swash edge and wave motion, the stationary background of each video frame is eliminated by computing the difference between each frame and the average of the frames over the previous 15 s (a time exposure). This technique shifts the visual emphasis from the immobile and unchanging parts of the scene to the moving and evolving components. Consequently, it enhances the overall quality of the output images, resulting in images for which the swash edge is easier to detect (Fig. 6).

V-BeachNet. To estimate swash motion, the video frames are fed to a new FCN model named V-BeachNet (Fig. 7) that has architecture following V-FloodNet (Liang et al., 2023), which was designed to detect water and flood in videos in urban areas (Liang et al., 2020b). Unlike V-FloodNet, which mainly focuses on still water in urban flooding, here it is necessary to process the moving waves running up and down the
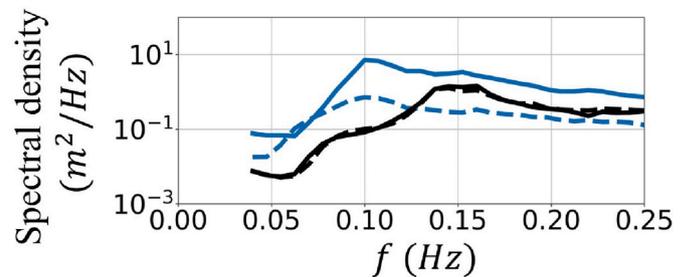

Fig. 3. Power spectral density of the incident wave field (1-h time series in ~9-m water depth) versus frequency for Case 1 (solid blue curve), Case 2 (dashed blue curve), Case 3 (solid black curve), and case 4 (dashed black curve).
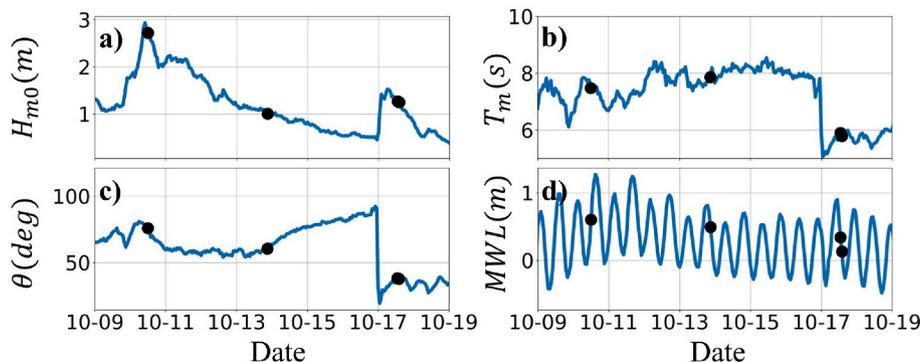

Fig. 2. Offshore (~9-m water depth) a) significant wave height, b) mean spectral period, c) mean wave direction, and d) (~6-m water depth) mean water level versus time. The four case studies are indicated by the black circles (the symbols for the 2 cases on October 17 overlap).
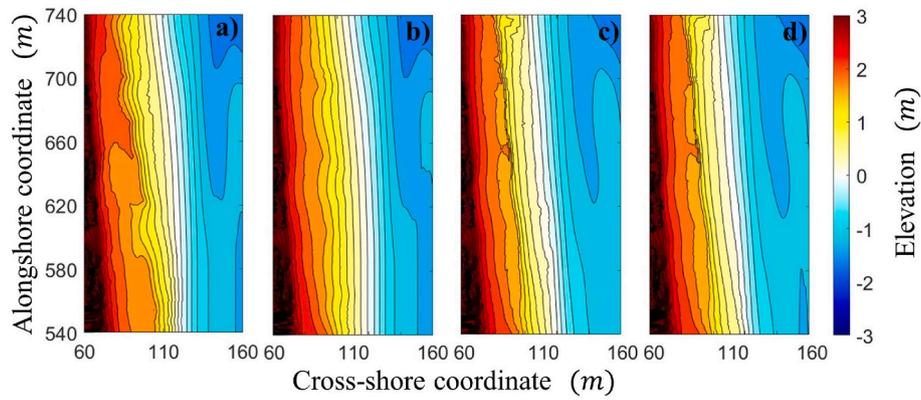
Fig. 4. Color contours (scale on the right, contour curves every 0.3 m) of topography and bathymetry elevations (relative to NAVD88, similar to mean sea level) within the camera fields of view as a function of cross- and alongshore coordinates for a) Case 1, b) Case 2, c) Case 3, and d) Case 4.
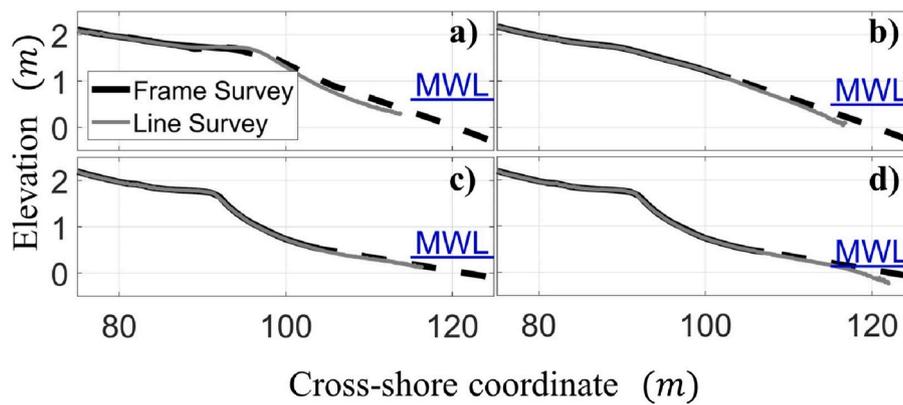

Fig. 5. Elevation along the cross-shore transect Y = 620 m estimated with cross-shore lidar scans (gray curves), the 3D lidar scans (black curves), and interpolated from vehicle surveys (dashed black curve, extending the lidar scans farther offshore) versus cross-shore coordinate for a) Case 1, b) Case 2, c) Case 3, and d) Case 4. MWL for each case is indicated with blue lines.
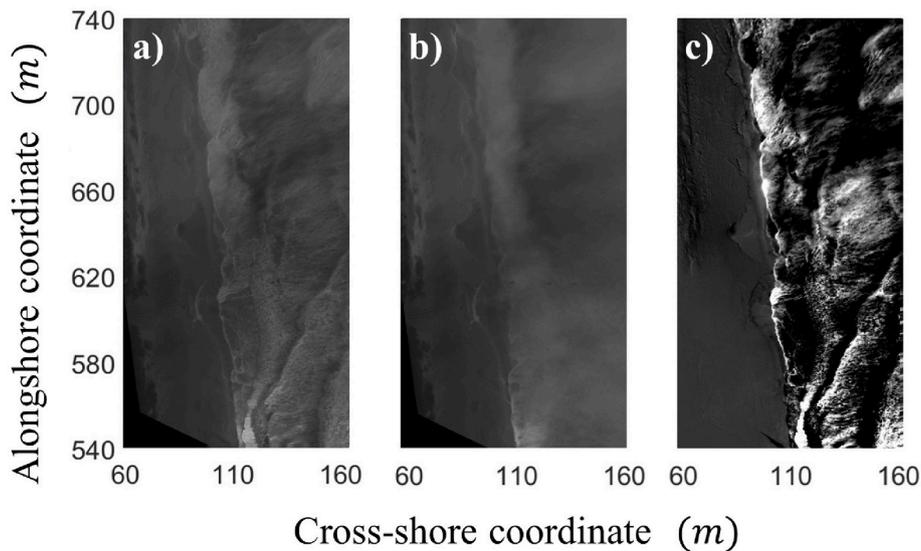

Fig. 6. a) A rectified image before processing, b) a time exposure image for the preceding 15 s, and c) processed image. Moving runup bores are highlighted with white color on the processed image.

beach in the swash zone. Moving waves evolve rapidly, and thus differentiating and identifying the swash edge from the sand using V-FloodNet is difficult and often unsuccessful. To address this issue, the V-BeachNet model was trained using rectified grayscale images of the

FRF beach to optimize its parameters for estimating swash. Image rectification not only reduces distortions to enhance model predictions, but also aligns images and bathymetry surveys within a consistent coordinate system that is essential for the runup estimation. Additionally,
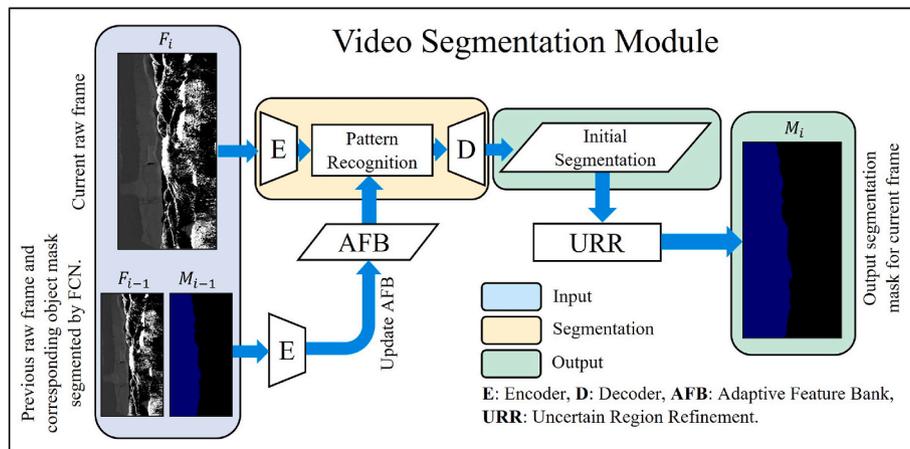
Fig. 7. Video segmentation module overview. Adaptive Feature Bank (AFB) updates the feature bank with information from the previous frame and mask. The segmentation module generates an initial segmentation. The Uncertain-Region Refinement (URR) technique further refines the segmentation.

grayscale images, possessing a single channel, not only significantly reduce computational costs compared with three-channel RGB images, but also excel in tasks where texture and shape segmentation is prioritized over color. The main idea and high-level explanation of V-Beach-Net is below, with more technical design details about flood video segmentation in two closely related previous studies (Liang et al., 2020a, 2023).

V-BeachNet employs the EfficientNet-B4 encoding architecture (Tan and Le, 2019) and the LinkNet decoding architecture (Chaurasia and Culurciello, 2017) as part of its video segmentation module. The encoding process extracts feature maps from the input video images using convolutional blocks. These feature maps encompass details about shapes, edges, textures, and patterns, learned by the neural networks. These maps are then transformed into pairs of *"key"* and *"value"*

embeddings. The *key* incorporates the essential characteristics of the feature map, enabling comparison of similarity between the feature maps of the query frame and the feature bank (that managed features of objects/regions observed in the previous frames of the video), while the *value* conserves the semantic information used to estimate the object mask. The decoding stage in V-BeachNet, leveraging the LinkNet decoding architecture, focuses on reconstructing the segmented images from the feature maps generated by the EfficientNet-B4 encoding process.

Two encoders are integrated into the segmentation module. One is utilized to encode the current frame (query frame) for segmentation. The other is employed to encode the previous frame (reference frame) and its corresponding mask for each object. Object-level feature maps of the reference frame are utilized to update the feature bank for each object.
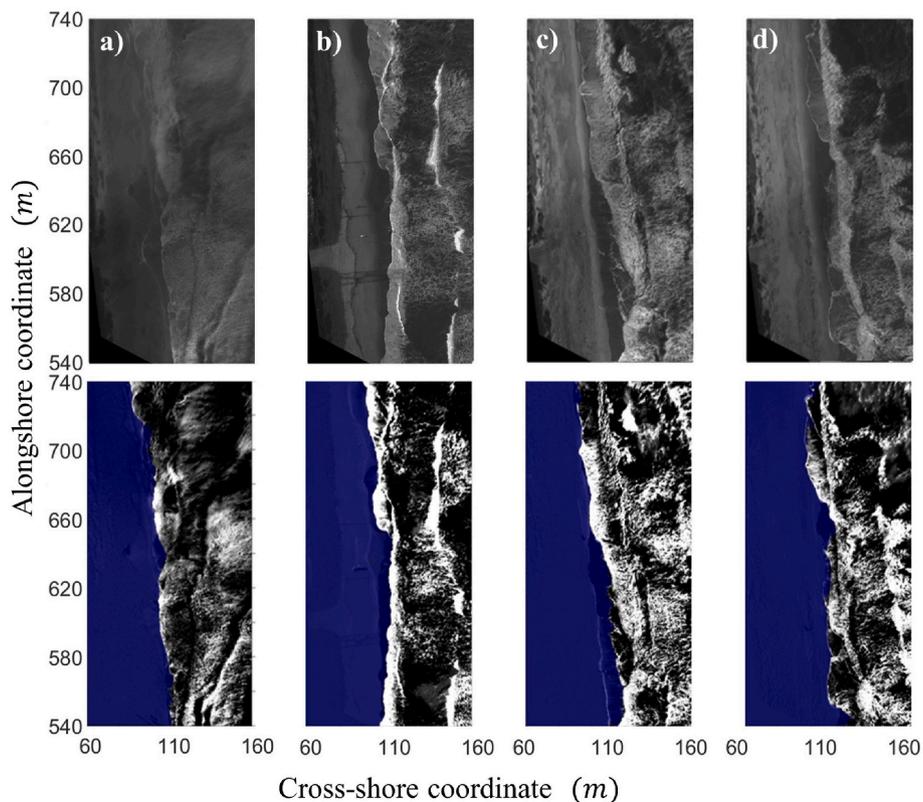

Fig. 8. Raw video frames (upper panels) and segmentation of processed video frames (lower panels) for a) Case 1, b) Case 2, c) Case 3, and d) Case 4.
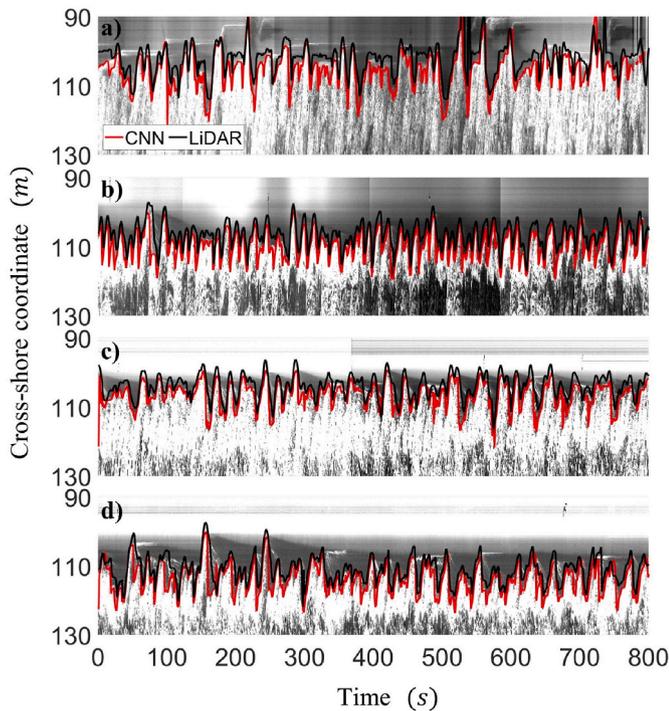
Fig. 9. Video imagery at Y = 620 m as a function of cross-shore coordinate and time, with the swash edge detected by the FCN model (solid red curves) and by lidar (solid black curves) for a) Case 1, b) Case 2, c) Case 3, and d) Case 4.

Fig. 10. Estimates of swash elevation from the FCN model (solid red curves) and lidar (solid black curves) versus time along the cross-shore transect at Y-620 m for a) Case 1, b) Case 2, c) Case 3, and d) Case 4. The RMSE values for the FCN model predictions for Cases 1 to 4 are: 0.33 m, 0.27 m, 0.15 m, and 0.14 m, respectively.

The *key* to the query frame is then matched with the most similar *key* in the feature bank for each object, and the corresponding *value* from the feature bank is retrieved. This retrieved *value* is concatenated with the query *value* to obtain the semantic information for each object. Subsequently, the decoder uses this semantic information to estimate the initial object mask by upscaling the feature maps through skip connections (He et al., 2016; Chaurasia and Culurciello, 2017) which connect the corresponding layers of the encoder and decoder.

V-BeachNet has two additional parts that are made specifically for handling long videos and utilizing information about the coherence of time and space in consecutive frames (Liang et al., 2020a). As mentioned before, features from the encoded reference frames are added to the feature bank at each time step. In long videos, the feature bank can become quite large, causing the segmentation task to slow down. To address this issue, the Adaptive Feature Bank (AFB) dynamically adjusts the learned features from reference frames and removes outdated features. This ensures that changes in the appearance of objects over time can be accurately tracked with optimal performance. The Uncertain Region Refinement (URR) module focuses on improving the segmentation of each frame after the initial segmentation, which is crucial for estimating runup accurately at the pixel level.

For training purposes, images were rectified and enhanced, then labeled with the LabelMe public open-source tool (Wada, 2016). V-BeachNet underwent training using sets of 4, 8, 16, and 32 manually segmented images, which were randomly selected from a dataset consisting of 28,800 video frames obtained during four 1-h periods (Table 1). Given the labor-intensive nature of manually labeling shoreline images, it is beneficial to train the model using a smaller dataset. While training time saw a 50% increase when the dataset size was doubled, the cross-entropy loss (Liang et al., 2020a) showed no significant improvement, recording values of 0.16, 0.12, 0.11, and 0.11 for the datasets of 4, 8, 16, and 32 images, respectively. Consequently, the model trained with 16 images was selected for subsequent analysis. The trained segmentation module efficiently extracts swash excursions along the entire alongshore extent of the beach (Fig. 8). It segments two frames
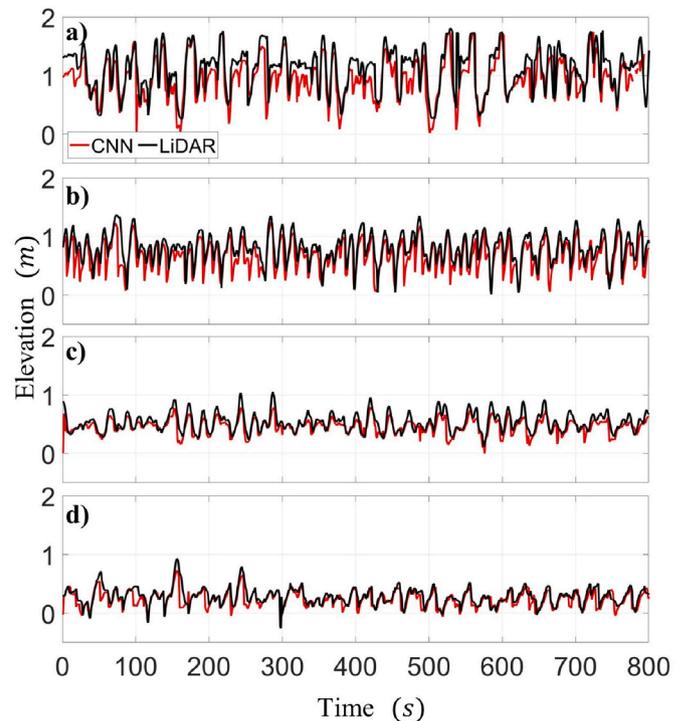
per second, enabling the real-time processing of 4 h of video imagery and highlighting its high computational efficiency.

3. Results

Estimates of the edge of the swash from the FCN model are in good agreement with those from the lidar (compare solid red with black curves near the swash edge in Fig. 9). The maxima and minima of the horizontal lidar-estimated swash are somewhat more onshore than the estimates from the FCN model (Fig. 9). Offshore-moving wave rundown is more transparent (less contrast), and thus harder to detect in images than the foamier onshore-propagating wave runup. Difficulty in detecting visual features with lower contrast is inherent to computer vision techniques and may be a source of error that results in lower wave setup and 2% runup exceedance estimated by the FCN model.

When converted to vertical swash, the lidar and FCN estimates align with each other (Fig. 10), although lidar-estimated swash is higher than FCN swash, consistent with differences in estimates of the horizontal locations (Fig. 9). The FCN estimates of rundown often are lower than the corresponding lidar estimates, especially in Cases 1 (Figs. 10a) and 2 (Fig. 10b). For Cases 3 and 4, rundown levels are similar in both methods (Fig. 10c and d). Taking LiDAR measurements as the standard for accuracy, the root mean square errors (RMSE) for the FCN model predictions in Cases 1 to 4 are 0.33, 0.27, 0.15, and 0.14 m, respectively. The differences in runup can be owing to errors in image rectification that assumed a flat surface, which would increase with increasing elevation above the flat plane (at $z = 0$). Most swash motions were above the flat plane, and thus rectification errors increase with swash excursion and beach slope. Consequently, the FCN model predictions show greater RMSE values for Case 1 and Case 2, which had larger swash motions, relative to Case 3 and Case 4. There also could be errors inherent to optical methods. To address these issues, future research could explore the use of color imagery, which might enhance the ability
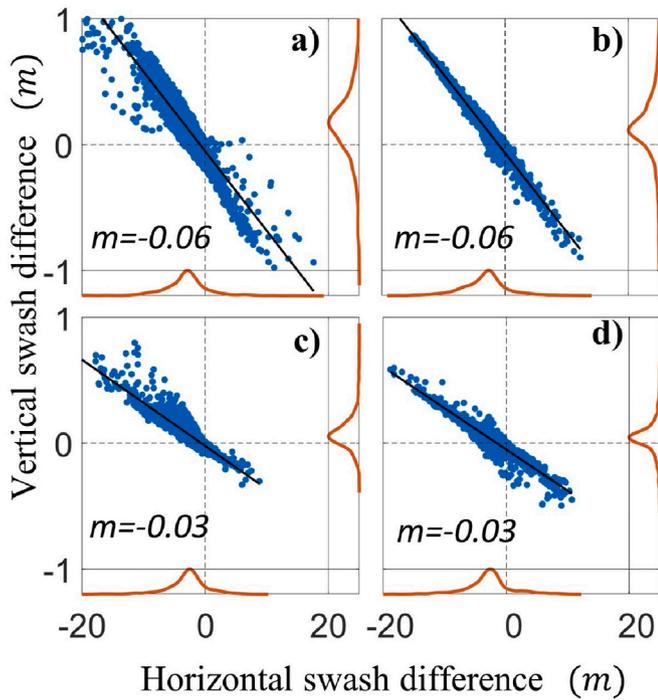
Fig. 11. Difference in vertical versus horizontal swash estimated by FCN and lidar for a) Case 1, foreshore slope β_f = -0.08, b) Case 2, β_f = -0.07, c) Case 3, β_f = -0.04, and d) Case 4, β_f = -0.04. The solid curve is the linear least squares fit and its slope is denoted by m in all panels. The red curves on each panel represent the probability density function for the horizontal swash (horizontal curves) and vertical swash (vertical curves) difference data points.

to distinguish between swash, foam, debris, and the beach backdrop, potentially reducing errors related to optical methods and improving bathymetry estimates. Moreover, the lidar scans occasionally encountered debris, remnant foam, or stagnant water, causing swash edge estimates to become temporarily fixed at the upper edge of the swash, leading to artificially increased swash elevations. Another potential source of error is noise in bathymetry estimates, including uncertainties introduced during lidar scanning due to fluctuating sand levels affecting the detection of the minimum water depth for swash edge determination.

Differences between V-BeachNet and lidar vertical swash estimates are small when differences in horizontal swash estimates are small, and differences in estimated vertical and horizontal swash excursions are well described by the beach slope (compare slope of best fit lines in Fig. 11 with the beach slope given in the caption), suggesting differences

in vertical swash are primarily owing to differences in estimating horizontal swash (e.g., not owing to inaccurate bathymetry). Furthermore, the FCN-estimated horizontal swash typically is offshore of the lidar estimate, consistent with errors owing to using a flat plane rectification (Fig. 11). The probability density functions of the difference data points for horizontal and vertical swash (horizontal and vertical red curves, respectively in Fig. 11) have maxima near 0, suggesting that although there are a few significant errors, the majority of the runup error points fall within an acceptable range.

Spectra of vertical swash time series estimated by the FCN Model are in good agreement with the spectra estimated from the lidar (Fig. 12). Although the lidar can estimate swash, it is limited to a single cross-shore transect. In contrast, the FCN model can estimate swash along the shoreline within the field of view of the cameras, and combined with the measurements of bathymetry can provide estimates of the along-shore variability of the vertical swash motion.

Swash spectral density demonstrates variation of swash motion along the 200 m stretch of the coastline (Fig. 13). In the infragravity band (frequency f < 0.05 Hz), Case 1 (Fig. 13a) has a strong variation with lower energy in the middle of the domain (roughly $620 < Y < 690$
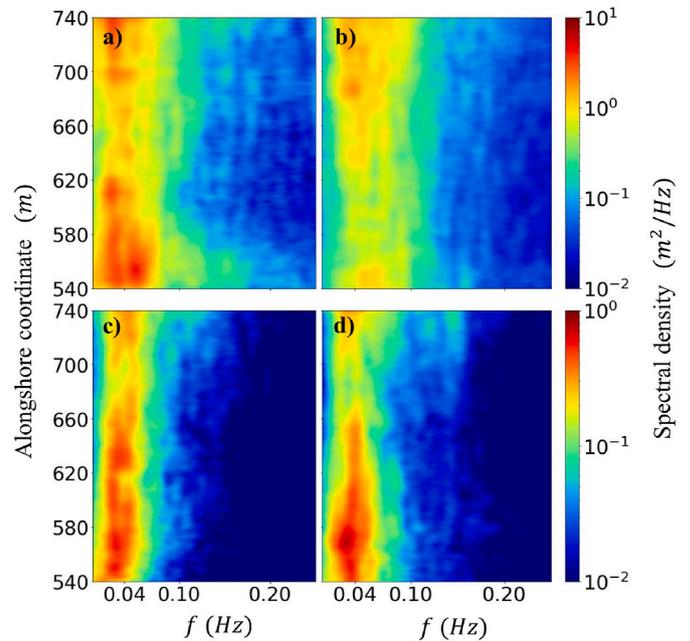

Fig. 13. Vertical swash spectral density (color contours, separate color bar for each row on the right) as a function of alongshore coordinate versus frequency for a) Case 1, b) Case 2, c) Case 3, and d) Case 4.
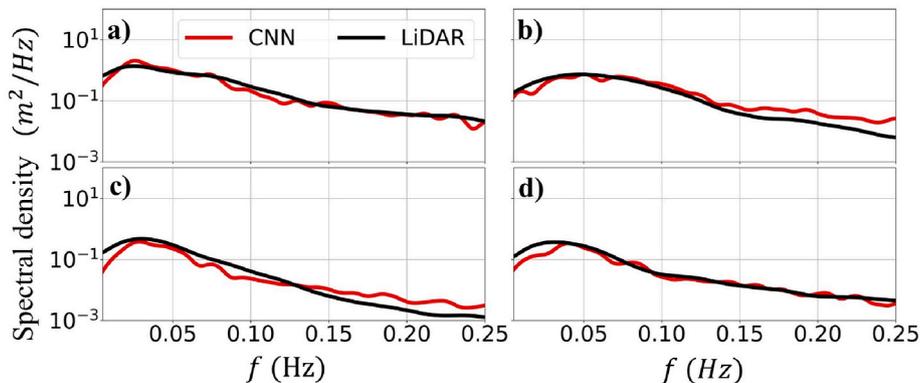

Fig. 12. Power spectral density of vertical swash estimated with FCN (red curves) and lidar (black curves) versus frequency at Y = 620 m for a) Case 1, b) Case 2, c) Case 3, and d) Case 4.
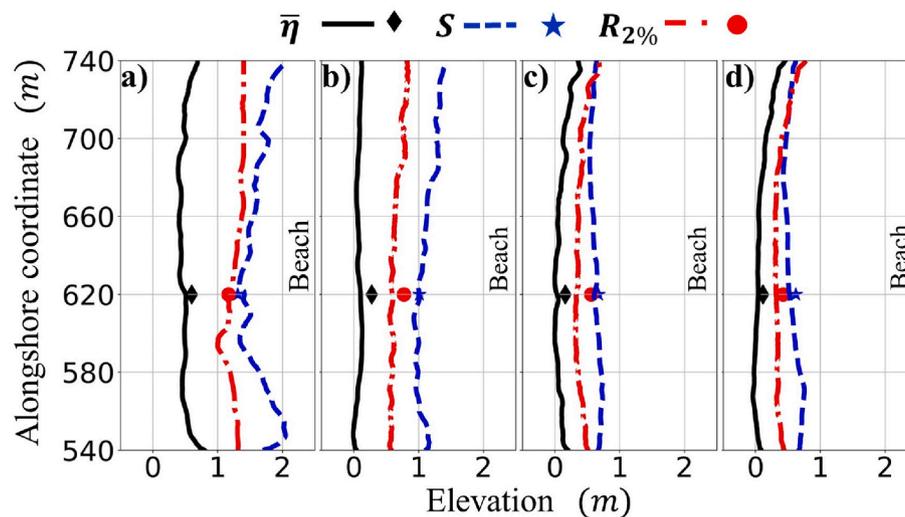
Fig. 14. FCN (curves) and lidar (symbols) estimated runup significant swash height (dashed blue curves, blue stars), the 2% exceedance value of runup (dash-dotted red curves, red circle), and setup (solid black curves, black diamond) as functions of alongshore coordinate and elevation for a) Case 1, b) Case 2, c) Case 3, and d) Case 4.

m). Case 2 (Fig. 13b) has higher energy at the north end of the region (Y > 680 m). Cases 3 and 4 also have minima in the infragravity swash energy at about Y = 690 and Y = 680 m, respectively (Fig. 13c and d). Similar to prior studies (Guedes et al., 2012), the causes of these alongshore variations of infragravity swash energy are uncertain. Alongshore variations in incident wave energy are believed to be small, but the energy patterns at least partly could be related to variable swash zone beach slopes (Fig. 3) or to variable infragravity generation and dissipation over the surfzone bathymetry (Holland and Puleo, 2001; Fiedler et al., 2015; Senechal et al., 2018).

There is good agreement between lidar and FCN measurements of wave-induced changes to the mean water level (setup), significant swash height (4 times the standard deviation of the vertical swash excursion), and the 2% exceedance value of runup at Y = 620, especially for Cases 1 and 4 (Fig. 14, compare symbols with same color curves). Setup often is nearly constant along the beach, except at the boundaries where it increases up to about 0.5 m (black curves in Fig. 14). The 2% runup exceedance also is nearly alongshore uniform (dash-dotted red curve in Fig. 14a), except near Y = 600 m, where it decreases. The significant swash height varies along the shore, with lower values in the middle of the domain (dashed blue curve in Fig. 14). This alongshore variation is strongest for Case 1 (1.2 < swash height <2.0 m), possibly owing to a larger alongshore variation in the swash zone beach slope or a magnification of the effects of the surfzone bathymetry (refraction, dissipation, and wave-current interactions) related to the larger offshore wave heights and incident directions (Fig. 2). Significant wave height, setup, and 2% exceedance wave runup are relatively uniform alongshore for Case 2 (Fig. 14b), as is the bathymetry (Fig. 4b). The FCN estimated significant swash height agrees well with the lidar estimate in Case 2 (compare the blue diamond with the blue dashed curve in Fig. 14b). However, FCN underestimates setup and the 2% exceedance runup (Fig. 14b). All three parameters are relatively uniform alongshore for Cases 3 and 4 (Fig. 14c and d). The alongshore pattern of the 2% exceedance runup is similar to the wave setup pattern, which increases to the north, possibly owing to wave focusing in this region, reduced wave dissipation where the sandbar is absent, or a steeper swash zone beach slope (Fig. 4).

4. Conclusions

The paper presents a new method to estimate swash excursion automatically from shoreline video frames using a deep learning framework with unique computer vision algorithms. The framework includes the processing of raw frames as inputs to the FCN model, the integration of bathymetric surveys to derive field-scale vertical swash, setup, and 2% runup exceedance values along a few 100 m of the sandy beach, and the analysis and identification of error sources in the extraction of swash motion from video imagery.

As a core part of this deep-learning framework, V-BeachNet, a FCN model that leverages advanced features such as Adaptive Feature Bank (AFB) and Uncertain-Region Refinement (URR), estimates swash excursions along the shoreline. The FCN model was trained with 16 randomly selected and manually segmented images of the swash zone, and then used to estimate swash excursions for four 1-h sets of 2 Hz images. FCN estimates of swash excursions can be degraded by errors introduced in video image rectification caused by the assumption of a flat surface, and by the difficulty of detecting rundown. However, despite potential errors, spectra of swash excursions, significant swash heights, wave setup, and the 2% exceedance values of runup estimated by the FCN model agree reasonably well with those estimated by a scanning lidar. Although the results are promising, improved image rectification and better synchronized topographic and bathymetric data would enhance the accuracy of wave runup extracted by the V-BeachNet.

V-BeachNet offers the capability to analyze archived, as well as real-time video footage, enabling the quantification of alongshore variation of swash motion on beaches that extend over hundreds of meters. By utilizing this deep-learning framework, the swash or runup data extracted from the videos can be paired with phase-resolving numerical modeling, providing a powerful tool for the study of swash zone dynamics.

CRediT authorship contribution statement

Reza Salatin: Writing – original draft, Validation, Software, Methodology, Investigation, Formal analysis, Data curation, Conceptualization. **Qin Chen:** Writing – review & editing, Validation, Supervision, Methodology, Funding acquisition, Conceptualization. **Britt Raubenheimer:** Writing – review & editing, Validation, Resources, Conceptualization. **Steve Elgar:** Writing – review & editing, Validation, Resources, Conceptualization. **Levi Gorrell:** Resources, Data curation. **Xin Li:** Writing – review & editing, Software.

Declaration of competing interest

The authors declare that they have no known competing financial interests or personal relationships that could have appeared to influence the work reported in this paper.

Data availability

Data will be made available on request.

Acknowledgments

References

Bentivoglio, R., Isufi, E., Jonkman, S.N., Taormina, R., 2022. Deep learning methods for flood mapping: a review of existing applications and future research directions. Hydrol. Earth Syst. Sci. 26 (16), 4345–4378.

Breiman, L., 2001. Random forests. Mach. Learn. 45, 5–32.

Chaurasia, A., Culurciello, E., 2017. LinkNet: exploiting encoder representations for efficient semantic segmentation. In: IEEE Visual Communications and Image Processing (VCIP), pp. 1–4.

Collins, A.M., O'Dea, A., Brodie, K.L., Bak, A.S., Hesser, T.J., Spore, N.J., Farthing, M.W., 2023. Automated extraction of a depth-defined wave runup time series from lidar data using deep learning. IEEE Trans. Geosci. Rem. Sens. 61, 1–13.

Cortes, C., Vapnik, V., 1995. Support-vector networks. Mach. Learn. 20, 273–297.

den Bieman, J.P., de Ridder, M.P., van Gent, M.R., 2020. Deep learning video analysis as measurement technique in physical models. Coast Eng. 158, 103689.

Dodd, N., 1998. Numerical model of wave run-up, overtopping, and regeneration. J. Waterw. Port, Coast. Ocean Eng. 124 (2), 73–81.

Drummond, C.D., Harley, M.D., Turner, I.L., Matheen, A.N.A., Glamore, W.C., 2015. UAV applications to coastal engineering. Australasian Coasts & Ports Conference 2015, 22nd.

Ellenson, A.N., Simmons, J.A., Wilson, G.W., Hesser, T.J., Splinter, K.D., 2020. Beach state recognition using argus imagery and convolutional neural networks. Rem. Sens. 12 (23), 3953.

Fiedler, J.W., Brodie, K.L., McNinch, J.E., Guza, R.T., 2015. Observations of runup and energy flux on a low-slope beach with high-energy, long-period ocean swell. Geophys. Res. Lett. 42 (22), 9933–9941.

Guedes, R.M., Bryan, K.R., Coco, G., 2012. Observations of alongshore variability of swash motions on an intermediate beach. Continent. Shelf Res. 48, 61–74.

Guza, R.T., Thornton, E.B., 1985. Observations of surf beat. J. Geophys. Res.: Oceans 90 (C2), 3161–3172.

He, K., Zhang, X., Ren, S., Sun, J., 2016. Deep residual learning for image recognition. In: Proceedings of the IEEE Conference on Computer Vision and Pattern Recognition, pp. 770–778.

Holland, K.T., Puleo, J.A., 2001. Variable swash motions associated with foreshore profile change. J. Geophys. Res.: Oceans 106 (C3), 4613–4623.

Holman, R.A., Sallenger, A.H., Lippmann, T.C., Haines, J.W., 1993. The application of video image processing to the study of nearshore processes. Oceanography 6 (3), 78–85.

Holman, R.A., Stanley, J., 2007. The history and technical capabilities of argus. Coast Eng. 54 (6–7), 477–491.

Hughes, M.L., McDowell, P.F., Marcus, W.A., 2006. Accuracy assessment of georectified aerial photographs: implications for measuring lateral channel movement in a GIS. Geomorphology 74 (1–4), 1–16.

Jafari, N.H., Li, X., Chen, Q., Le, C.Y., Betzer, L.P., Liang, Y., 2021. Real-time water level monitoring using live cameras and computer vision techniques. Comput. Geosci. 147, 104642.

Jensen, A., Pedersen, G.K., Wood, D.J., 2003. An experimental study of wave run-up at a steep beach. J. Fluid Mech. 486, 161–188.

Kirillov, A., Mintun, E., Ravi, N., Mao, H., Rolland, C., Gustafson, L., Xiao, T., Whitehead, S., Berg, A.C., Lo, W.Y., Dollár, P., 2023. Segment Anything arXiv preprint arXiv:2304.02643.

Krizhevsky, A., Sutskever, I., Hinton, G.E., 2012. ImageNet classification with deep convolutional neural networks. Adv. Neural Inf. Process. Syst. 25.

LeCun, Y., Bengio, Y., Hinton, G., 2015. Deep learning. Nature 521 (7553), 436–444.

Liang, Y., Jafari, N., Luo, X., Chen, Q., Cao, Y., Li, X., 2020b. WaterNet: an Adaptive Matching Pipeline for Segmenting Water with Volatile Appearance, vol. 6. Computational Visual Media, pp. 65–78.

Liang, Y., Li, X., Jafari, N., Chen, J., 2020a. Video object segmentation with adaptive Feature Bank and uncertain-region refinement. Adv. Neural Inf. Process. Syst. 33, 3430–3441.

Liang, Y., Li, X., Tsai, B., Chen, Q., Jafari, N., 2023. V-FloodNet: a video segmentation system for urban flood detection and quantification. Environ. Model. Software 160, 105586.

Long, J., Shelhamer, E., Darrell, T., 2015. Fully convolutional networks for semantic segmentation. In: Proceedings of the IEEE Conference on Computer Vision and Pattern Recognition, pp. 3431–3440.

O'Dea, A., Brodie, K.L., Hartzell, P., 2019. Continuous coastal monitoring with an automated terrestrial lidar scanner. J. Mar. Sci. Eng. 7 (2), 37.

Raubenheimer, B., Guza, R.T., Elgar, S., Kobayashi, N., 1995. Swash on a gently sloping beach. J. Geophys. Res.: Oceans 100 (C5), 8751–8760.

Ruggiero, P., Komar, P.D., McDougal, W.G., Marra, J.J., Beach, R.A., 2001. Wave runup, extreme water levels and the erosion of properties backing beaches. J. Coast Res. 407–419.

Salatin, R., Chen, Q., Bak, A.S., Shi, F., Brandt, S.R., 2021. Effects of wave coherence on longshore variability of nearshore wave processes. J. Geophys. Res.: Oceans 126 (11), e2021JC017641.

Senechal, N., Coco, G., Plant, N., Bryan, K.R., Brown, J., MacMahan, J.H., 2018. Field observations of alongshore runup variability under dissipative conditions in the presence of a shoreline sandwave. J. Geophys. Res.: Oceans 123 (9), 6800–6817.

Stockdon, H.F., Holman, R.A., Howd, P.A., Sallenger Jr, A.H., 2006. Empirical parameterization of setup, swash, and runup. Coast Eng. 53 (7), 573–588.

Stockdon, H.F., Thompson, D.M., Plant, N.G., Long, J.W., 2014. Evaluation of wave runup predictions from numerical and parametric models. Coast Eng. 92, 1–11.

Suhayda, J.N., 1974. Standing waves on beaches. J. Geophys. Res. 79 (21), 3065–3071.

Tan, M., Le, Q., 2019. EfficientNet: rethinking model scaling for convolutional neural networks. In: International Conference on Machine Learning. PMLR, pp. 6105–6114.

Vousdoukas, M.I., Velegrakis, A.F., Dimou, K., Zervakis, V., Conley, D.C., 2009. Wave run-up observations in microtidal, sediment-starved pocket beaches of the eastern mediterranean. J. Mar. Syst. 78, S37–S47.

Wada, K., 2016. LabelMe: Image Polygonal Annotation with Python.

Xie, D., Zou, Q.P., Mignone, A., MacRae, J.D., 2019. Coastal flooding from wave overtopping and sea level rise adaptation in the northeastern USA. Coast Eng. 150, 39–58.

Yang, H., Zhang, C., Shi, J., Cao, X., Li, Y., 2022. Laboratory observations of swash signatures using video imagery. J. Mar. Sci. Eng. 10 (12), 1833.